Yaw Torque Authority for a Flapping-Wing Micro-Aerial Vehicle

Rebecca Steinmeyer, Nak-seung P. Hyun, E. Farrell Helbling, and Robert J. Wood

Abstract—Flapping-wing micro-aerial vehicles rely on subtle changes in the kinematics of high-frequency wing flapping to produce roll, pitch, and yaw torques. To generate yaw torque, the Harvard RoboBee changes the ratio of upstroke to downstroke speed ("split-cycling") by applying a second harmonic to the fundamental flapping signal for each wing. However, since flapping typically occurs near resonance (for efficiency), these higher harmonics are filtered out by the transmission and actuator dynamics. Therefore, reliable yaw control authority has proven elusive. We propose a method to generate yaw torque sufficient for in-flight control by using split-cycle flapping in an "iso-lift" regime, to mitigate resonant filtering by decreasing the flapping frequency and increasing the drive voltage, which produces lift identical to typical flight conditions. We model the expected torque at iso-lift conditions and apply this method to the physical RoboBee, achieving reliable, controllable yaw torque. Finally, we demonstrate yaw control with a simple heading controller, achieving a step response with a time constant an order of magnitude faster than previous attempts.

I. INTRODUCTION

The recent advent of micro-aerial vehicles (MAVs) has allowed controlled flight at historically prohibitive scales, while also presenting a new realm of challenges for power, sensing, and control [1], [2]. To achieve the necessary force and torque authority for flight at this scale, researchers seek inspiration from biological systems in the development of insect-inspired robots [3], [4], [5]. For example, the Harvard RoboBee [6] is an 80 mg MAV which achieves flapping-wing flight by applying sinusoidal signals to two piezoelectric bimorph actuators [7].

The RoboBee has achieved controlled flight [8] and has demonstrated torque production in roll, pitch, and yaw [9] (see Fig. 1 for axes definitions), but yaw torque is historically the weakest [10]. As such, roll and pitch torques are applied to perform lateral maneuvers, and direct yaw control is largely ignored [8]. While lateral control may be achieved in this manner, the lack of yaw control limits the capabilities of these vehicles; for example, yaw control is necessary for heading stabilization. One promising method for yaw torque production, particularly for under-actuated vehicles such as the RoboBee, is called "split-cycling"; that is, varying the relative speeds of the wing upstroke and downstroke to produce a net drag [11], as shown in Fig. 2. The wingstroke is determined by a sinusoidal signal sent to the actuators, with stroke kinematics passively determined by the transmission,

The authors are with the John A. Paulson School of Engineering and Applied Sciences, Harvard University, Cambridge, MA 02138, USA, and the Wyss Institute for Biologically-Inspired Engineering, Harvard University, Boston, MA 02115, USA, rhsteinmeyer@g.harvard.edu, nphyun@g.harvard.edu, ehelbling@seas.harvard.edu, rjwood@eecs.harvard.edu.

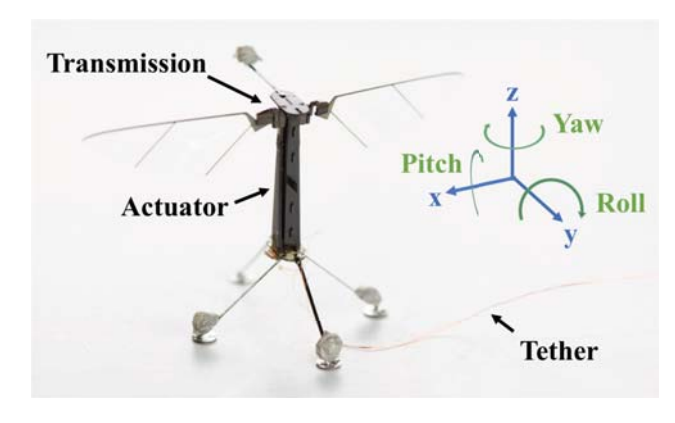


Fig. 1. The Harvard RoboBee, with defined rotational axes.

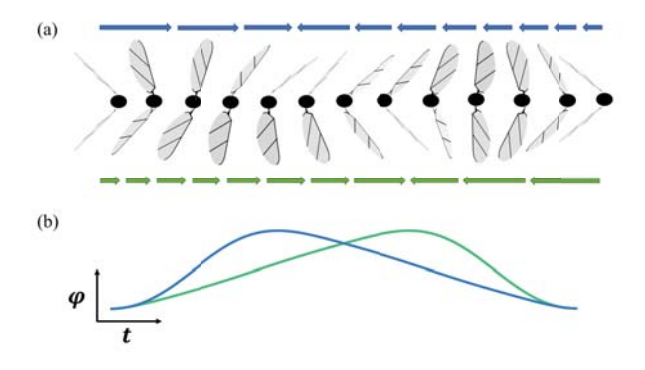


Fig. 2. Split-cycle wing-flapping is used to induce a net drag to produce yaw torque. (a) A full split-cycle wing stroke; blue and green arrows indicate the transition from upstroke to downstroke for each wing. (b) An example of paired split-cycle wingstroke motions; blue and green lines correspond to stroke angles of the wings shown above.

hinge, and wing. Although this method has been applied in a basic demonstration of yaw control for the dual-actuator RoboBee [12], it required almost a full second for a 90-degree turn, and performance was heavily affected by local airflow in the indoor test arena. As such, RoboBee yaw authority is not sufficient for robust control and aggressive maneuvers. While strategies have been proposed to improve yaw control authority (including active control of the wing angle-of-attack using an additional actuator [13] and sleeve-stop hinges to vary the wing stiffness profile [10]), a solution which does not substantially complicate manufacturing and which produces controllable torque at lift conditions has not yet been found.

Since the RoboBee transmission (Fig. 1) acts as a low-pass filter at frequencies higher than the flapping resonant frequency ([9], [14], [15]), and the split-cycle method produces

a difference between upstroke and downstroke speed by applying higher-order harmonics to the wingstroke sinusoid [16], we may infer that poor yaw control authority is the result of filtering of the higher harmonics in the split-cycle command. As such, at the operating frequency and voltage applied for efficient flight, yaw torques become negligible and effectively useless.

In this work, we propose a method to produce yaw torque sufficient for aggressive maneuvering via split-cycling combined with simultaneous frequency and voltage modulation. Yaw torque is produced by shifting the operating conditions to a state of lower frequency and higher voltage (such that lift remains consistent with normal flight: "isolift" conditions) during split-cycling to reduce the attenuation of the higher-order harmonics of the split-cycle sinusoid. Applying this method, we achieved yaw torques sufficient for aggressive maneuvering under conditions suitable for flight (i.e., reliable yaw torques which allow full revolutions within tenths of a second), and implemented this technique in simple heading control, demonstrating a step response an order of magnitude faster than previously achieved on the dual-actuator RoboBee.

II. YAW TORQUE MODELING

We developed a model to explore the stroke angle frequency response. In addition to predicting resonance and regions conducive to efficient flight, the model also predicts the filtering of higher-order sinusoids (i.e., filtering of the splitcycle effect through the transmissions and actuators). We also modeled thrust forces and axial torques to predict the ideal (unfiltered) control authority at given operating conditions. We then combined the torque and force models with the transmission-actuator transfer function to predict the forces and torques produced by the RoboBee to demonstrate the filtering of the split-cycle effect for yaw torque generation.

A. Split-Cycle Filtering

We first derived a second-order transfer function to describe the frequency-dependent relationship between the actuator drive voltage and the resulting flapping motion, following the approach applied in [15] and [17]. Note that the most accurate model for the current RoboBee is found in [14]; however, we will instead use the simpler second-order model, which provides sufficient fidelity and matches the key features of the model in [14], including the resonant frequency and high frequency roll-off. Physical parameters from [14], [15], and [17] (actuator mass m_a , actuator and transmission stiffnesses k_a and k_t , damping b, transmission ratio T, shoulder length r_{cp} , and moment of inertia J_{ϕ}) are incorporated into the model and appear in Table I.

We modeled the transmission and actuator combination as a spring-mass-damper system with m_{eq} , b_{eq} , and k_{eq} (equivalent mass, damping, and stiffness, respectively) with respect to the flapping frequency ω . The transfer function $H(\omega)$ represents the relationship between the voltage input signal, $V(\omega)$, and the wing stroke angle, $\Phi(\omega)$, in the

 $\label{eq:TABLE} TRANSMISSION \ \text{AND ACTUATOR MODELING PARAMETERS}$

Actuator mass	m_a	25 mg
Wing moment of inertia	J_{ϕ}	51.1 mg·mm ²
Transmission ratio	T	2666
Shoulder length	r_{cp}	1.42 × 9.56 mm
Aerodynamic damping	b	$2.03 \times 10^{-6} \mu\text{Ns/m}$
Actuator stiffness	k_a	300 N/m
Transmission stiffness	k_t	28.2 μNm/rad
Equivalent mass	m_{eq}	0.388 g
Equivalent damping	b_{eq}	0.196 Ns/m
Equivalent stiffness	k_{eq}	500.4 N/m

frequency domain, which is scaled with a gain A_H such that $H(\omega) = \Phi(\omega)/V(\omega)$:

$$H(\omega) = \frac{A_H}{m_{eq}(\omega i)^2 + b_{eq}(\omega i) + k_{eq}}$$
(1)

The constants m_{eq} , b_{eq} , and k_{eq} , calculated as described in [17], are given in Table I, as well as all parameters required for their calculation. The resulting frequency response is shown in Fig. 3, also indicating the typical flapping frequency range used for flight (chosen for its proximity to resonance, resulting in high-amplitude flapping), and the proposed operating regime. The resulting split-cycle filtering effect is shown in Fig. 4.

A harmonic voltage input signal is considered and given as $V(t) = V_{amp} \psi(t)$ where $2V_{amp}$ is the peak-to-peak voltage and ψ represents the shape of the harmonics with a fundamental frequency ω and coefficients a_1 , a_2 , and a_3 corresponding to the first three harmonics:

$$\psi(t) = a_1 \sin(\omega t) \pm a_2 \sin(2\omega t) + a_3 \sin(3\omega t). \tag{2}$$

The coefficients, a_1 , a_2 , and a_3 , are chosen such that

$$\max_{t \in (-\pi/\omega, \pi/\omega)} |\psi(t)| = 1 \tag{3}$$

holds. The stroke angle ϕ may then be described by transforming V to $H(\omega)$ using (1):

$$\phi(t) = V_{amp} \sum_{n=1}^{3} a_n |H(n\omega)| \sin(n\omega t - \angle H(n\omega))$$
 (4)

where $\angle H(n\omega)$ is the phase of the system evaluated at frequency $n\omega$. For our purposes, the fundamental frequency is the primary wingbeat frequency of the MAV, the second harmonic is responsible for the split-cycle effect (the variation in the ratio of upstroke to downstroke speed), and the third harmonic serves to flatten the signal, to allow higher-amplitude fundamental flapping frequencies and to smooth the signal after adding a second harmonic.

B. Force and Torque Modeling

The lift force generated by a wing flapping with stroke angle $\phi(t)$ may be calculated as follows [9], for a wing flapping in air with density ρ , with wingshape parameter

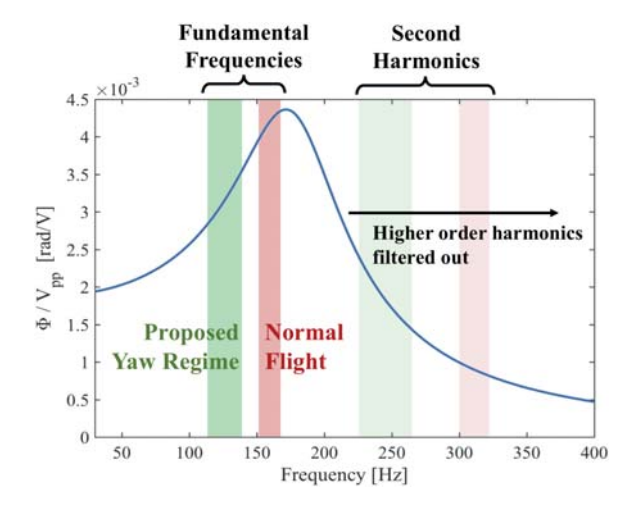


Fig. 3. A frequency response demonstrating wingstroke angle amplitude at different operating conditions, predicting significant filtering (via the actuator and transmission) of higher-order harmonics. The proposed isolift split-cycle method requires a lower fundamental frequency than normal flight, resulting in lower filtering of the second harmonic, and therefore an increase in yaw torque.

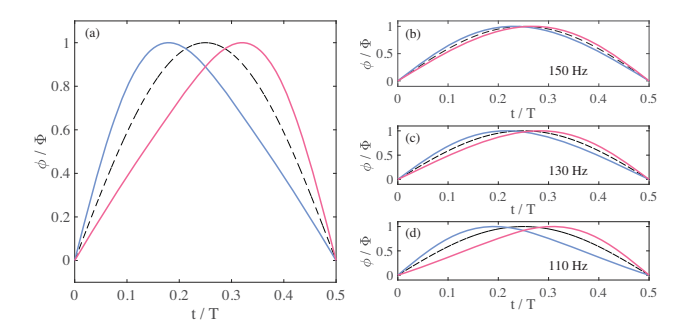


Fig. 4. Filtering of yaw-generating wingstroke signals through the actuator and transmission: An unfiltered signal is shown in (a), with corresponding filtered signals at 150Hz (b), 130Hz (c), and 110Hz (d) according to the transfer function presented in Fig. 3.

 β (as described in [18]) and lift coefficient $C_L(\alpha)$ (where α is the wing angle-of-attack) [19]:

$$F_L = \frac{1}{2} \rho \beta C_L(\alpha) \dot{\phi}^2. \tag{5}$$

Similarly, the drag force is expressed as

$$F_D = \frac{1}{2} \rho \beta C_D(\alpha) \dot{\phi} |\dot{\phi}| \tag{6}$$

where $C_D(\alpha)$ is the drag coefficient.

With shoulder length r_{cp} (see Fig. 1 and Table I), the yaw torque for a single wing may be calculated as follows:

$$\tau_{yaw} = \frac{1}{2} r_{cp} \rho \beta C_D(\alpha) \dot{\phi} |\dot{\phi}|. \tag{7}$$

We may calculate the time-averaged lift force for a single

wing, F_L^{avg} , using the wingstroke period $T = \frac{\omega}{2\pi}$:

$$F_L^{\text{avg}} = \frac{\omega}{2\pi} \int_0^{\frac{2\pi}{\omega}} F_L dt \tag{8}$$

$$= \frac{\omega}{4\pi} \rho \beta C_L \int_0^{\frac{2\pi}{\omega}} \dot{\phi}^2 dt \tag{9}$$

$$=\frac{1}{4}\rho\beta C_L(\omega V_{amp})^2\sum_{n=1}^3n^2(a_n|H(n\omega)|)^2. \tag{10}$$

Similarly, the time-averaged yaw torque τ_{yaw}^{avg} for a single wing may be calculated as:

$$\tau_{yaw}^{\text{avg}} = \frac{\omega}{2\pi} \int_0^{\frac{2\pi}{\omega}} \tau_{yaw} dt \tag{11}$$

$$= \frac{\omega}{4\pi} r_{cp} \rho \beta C_D \int_0^{\frac{2\pi}{\omega}} \dot{\phi} \left| \dot{\phi} \right| dt. \tag{12}$$

Note that total thrust equates to the sum of lift forces from each wing, and total yaw torque is the sum of yaw torques from each wing.

Considering the expressions for F_L^{avg} and τ_{yaw}^{avg} , we note that apart from the wingstroke $\phi(t)$, both expressions have the same relationship with non-constant parameters (that is, V_{amp} and ω). For our purposes, this means that if the split-cycle effect (due to wingstroke shape $\psi(t)$ within $\phi(t)$) is filtered by the transmission and actuator (modeled according to $H(\omega)$), yaw torque cannot be increased without simultaneously increasing the lift force, though the two are intended to be independent.

C. Iso-lift Conditions

We now define "iso-lift conditions" as the set of operating voltage, frequency, and shape parameters which result in equivalent time-averaged lift force. We propose that, during yaw maneuvers, the RoboBee shift to a lower-frequency iso-lift condition, thereby reducing split-cycle filtering due to the post-resonance roll-off and allowing independence between yaw and lift. Effectively, we predict that a lower operating frequency and higher applied voltage will permit yaw torque while maintaining a desired lift.

Let $p_A := (V_A, \omega_A, a_1, a_2, a_3)$ and $p_B := (V_B, \omega_B, b_1, b_2, b_3)$ be two sets of parameters used to generate time-averaged lift forces $F_L^{avg}(p_A)$ and $F_L^{avg}(p_B)$, respectively, by calculating lift using (10), and let $h : \mathbb{R}^5 \to \mathbb{R}$ be defined as

$$h(p_A, p_B) = F_L^{avg}(p_A) - F_L^{avg}(p_B).$$
 (13)

Then p_A and p_B satisfy the iso-lift condition if and only if $h(p_A, p_B) = 0$ holds, or equivalently, if and only if

$$\sum_{n=1}^{3} n^2 \left(\left(\omega_A V_A a_n |H(n\omega_A)| \right)^2 - \left(\omega_B V_B b_n |H(n\omega_B)| \right)^2 \right) = 0$$
(14)

holds. The above definition gives an equivalence relation, namely $p_A \sim p_B$, and the set of parameters can be partitioned by its equivalence class. An example of sets of parameters in the same equivalence class are shown in Table II; each set generates the same time-averaged lift force.

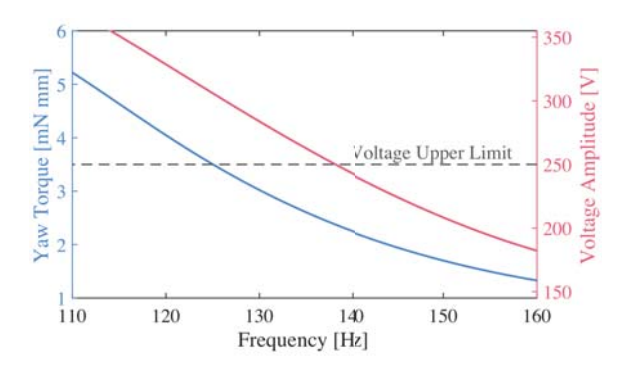


Fig. 5. Yaw torque (blue) increase at lower operating frequencies at iso-lift conditions, with required voltage shown in red. We impose a voltage limit for RoboBee wing-flapping to promote system longevity; higher voltages can cause damage to the actuators.

To model the effect of operating at iso-lift conditions on the resulting yaw torque, we first set a baseline lift condition: an efficient (i.e., close to resonance [6]) frequency, voltage, and shape combination with no second harmonic (and therefore no split-cycle effect, and no yaw torque). For the MAV used in these experiments, this baseline condition is a 150 Hz flapping frequency, 180 V drive voltage, and shape defined by sinusoid harmonic coefficients $(a_1 \ a_2 \ a_3) = (1.09 \ 0 \ 0.10)$; this achieves sufficient lift for takeoff of the RoboBee. (Note that flight conditions vary slightly between MAVs due to manufacturing imperfections and for an MAV over its lifespan as it experiences flexure wear [20]).

Based on these operating conditions and the previously-defined model for calculating lift and torque with split-cycle filtering, a plot of iso-lift conditions is shown in Fig. 5, with a defined acceptable operating voltage cutoff. The actuators for this RoboBee were tested up to 300 V, and are typically operated under 200 V; therefore, 250 V was set as a maximum allowable voltage during these experiments.

III. TORQUE GENERATION EXPERIMENTS

We conducted open-loop yaw velocity measurements at a set of iso-lift conditions equivalent in thrust to RoboBee hovering conditions, in line with the described model.

We applied positive and negative yaw torque conditions, along with a baseline (no yaw) flight condition, at a set of decreasing frequencies, and calculated a flapping signal sinusoid for each wing with the following structure, such that $\phi_N(t)$ corresponds to baseline conditions, and $\phi_Y(t)$ corresponds to yaw conditions. V_A , ω_A , and $\begin{pmatrix} a_1 & a_2 & a_3 \end{pmatrix}$ correspond to the baseline condition voltage, flapping frequency, and shape parameters, respectively; similarly, V_B , ω_B , and $\begin{pmatrix} b_1 & b_2 & b_3 \end{pmatrix}$ correspond to the yaw condition voltage, flapping frequency, and shape parameters (experimental parameters are provided in Table II).

$$\phi_N(t) = V_A \left[a_1 \sin(\omega_A t) + a_2 \sin(2\omega_A t) + a_3 \sin(3\omega_A t) \right]$$
 (15)

$$\phi_Y(t) = V_B \left[b_1 \sin(\omega_B t) \pm b_2 \sin(2\omega_B t) + b_3 \sin(3\omega_B t) \right]$$
 (16)

The positive and negative coefficients for the second harmonic for yaw, b_2 , will produce positive and negative



Fig. 6. Wing kinematics are maintained for iso-lift conditions at 140 Hz with a RoboBee operating in typical flight conditions (a) and iso-lift yaw conditions (b).

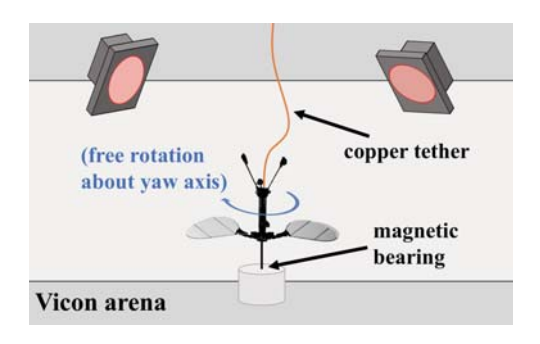


Fig. 7. Experimental setup for yaw torque measurements: The RoboBee is fixed upside-down in a Vicon arena via a magnetic bearing, which allows full rotation about its yaw axis. Note that a copper tether is attached to the MAV to provide power and control signals; the RoboBee must overcome torque from the tether and friction from the bearing in order to rotate.

torques, respectively.

Before conducting yaw torque experiments, we observed wingstroke kinematics for the RoboBee at iso-lift conditions to confirm that iso-lift yaw parameters would be flightworthy (to supplement the lift calculations in Section II), applying normal flight signals and iso-lift yaw signals at 140 Hz, with corresponding parameters found in Table II). As shown in Fig. 6, sufficient similarity exists in stroke kinematics between the iso-lift baseline flight and yaw torque operating conditions to confirm similar flight conditions between the two (thereby affirming validity of the iso-lift condition model).

During our experiments, we constrained the RoboBee to a single degree of freedom (i.e., rotation about the yaw axis) such that it could rotate freely; the experimental setup is shown in Fig. 7. We measured angular displacement using Vicon motion-capture cameras (Vicon T040 System, Oxford

TABLE II Torque Experimental Parameters

			~ 1	U Z	03
(Coefficients) 1.09	0	0.099	0.934	0.216	0.047

[1/]	x 7 [x 7]	x 7 [x 7]
$\omega_{A,B}$ [rad/s]	V_A [V]	$V_B \ [\mathrm{V}]$
$140 \cdot 2\pi$	210.9	242.8
$145 \cdot 2\pi$	194.5	224.6
$150 \cdot 2\pi$	180.0	208.3
$155 \cdot 2\pi$	167.5	194.1

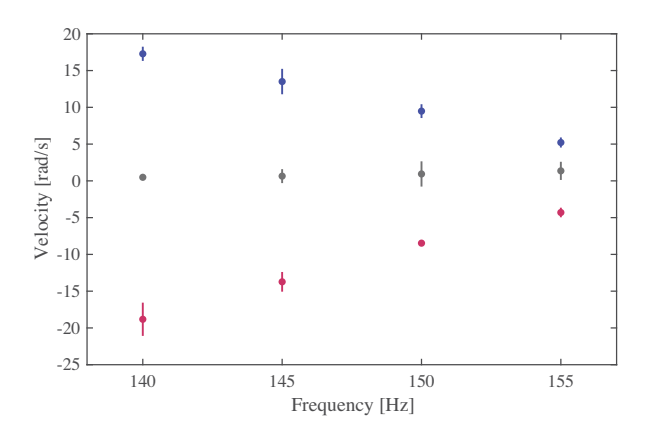


Fig. 8. Measured open-loop yaw velocities across a selection of isolift operating conditions. Velocities from positive and negative yaw torque are shown in blue and red, respectively; the baseline condition (no yaw torque applied) is shown in gray. Each data point represents an average measurement, with standard deviations shown by error bars. Four samples were taken for all yaw conditions and 145Hz-155Hz baseline conditions; two samples were taken for the 140Hz baseline condition.

UK) operating at 500 Hz. We applied a voltage-ramped signal with a duration of 0.4 s (0.1 s of linear ramping up and down; 0.2 s at full voltage) for each experiment; this corresponds to between 56 and 62 periods (at 140 Hz and 155 Hz, respectively).

We quantified the increase in yaw torque by measuring the time-varying angular velocity about the yaw axis. (We provide the average velocity in lieu of a direct measure of torque because this quantity is the clearest yaw torque metric provided directly by our motion capture methods.) At the maximum torque condition (with split-cycle shape defined in Table II), the MAV achieves an average of 17.28 rad/s and -18.82 rad/s, with corresponding standard deviations of 0.97 rad/s and 2.26 rad/s, for positive and negative yaw angular velocities over the full ramped (peak voltage) signal, respectively. This corresponds to angular displacements of 4.56 rad and -4.29 rad (with standard deviations of 0.59 rad and 0.74 rad) over 0.2 s at full voltage. We note that yaw torque magnitudes may be calculated from the motion capture data by considering the observed dynamics of the MAV in conjunction with ambient effects, including drag, tether effects, and bearing friction. While a full model of these effects is outside of the scope of this work, we note that the linear increase in velocity observed with increased applied yaw torque during experiments corresponds directly with the modeled vaw torque increase shown in Fig. 5.

Applying the iso-lift split cycle method for yaw torque generation, the RoboBee can accomplish a full rotation in a fraction of a second at flight conditions. This degree of yaw torque authority is sufficient for aggressive maneuvering, and therefore we proceed in implementation of an associated yaw controller.

IV. YAW CONTROL DEMONSTRATION

After demonstrating sufficient yaw torque authority for aggressive control, we demonstrate basic implementation of iso-lift split-cycle yaw torque in a simple heading controller.

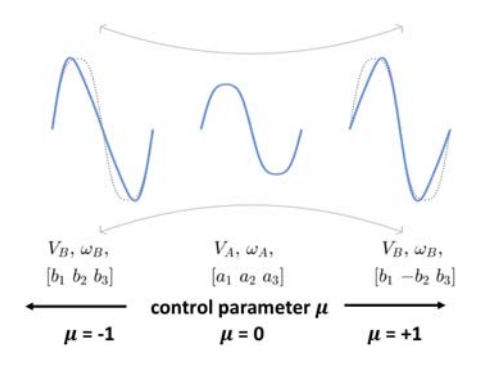


Fig. 9. A smooth multi-modal control parameter for yaw control. The parameter μ interpolates between iso-lift conditions: peak-to-peak signal voltage (V_A, V_B) ; flapping frequency (ω_A, ω_B) ; and sinusoid shape $(a_1, a_2, a_3; b_1, b_2, b_3)$, corresponding to amplitudes of the first, second, and third harmonics of a sinusoid at the fundamental operating frequency), centered on standard efficient flight (A) and extending to conditions of maximal positive and negative yaw torque (B).

We simplified the controller design by reducing the five-parameter set of signal sinusoid properties, as in (15) and (16), to a single parameter. This parameter μ , visualized in Fig. 9, scales from -1 to 1 such that the extremes correspond to maximum negative and positive yaw torque, respectively, and the zero-point is normal, efficient flight. Iso-lift conditions are maintained across the full span of μ .

The parameters used in these experiments at $\mu=0$ and $\mu=\pm 1$ are provided in Table III, which are at sub-hovering iso-lift conditions compared to the baseline conditions in Table II. To generate a continuous transition between yaw torques while preserving the iso-lift condition, a convex combination between (V_A,a_1,a_2,a_3) and (V_B,b_1,b_2,b_3) is considered by varying the parameter μ from [0,1], and a convex combination between $(V_B,b_1,-b_2,b_3)$ and (V_A,a_1,a_2,a_3) with μ varying from [-1,0]. If we denote $(V_\mu,c_{\mu 1},c_{\mu 2},c_{\mu 3})$ as the new parameter set for a given μ , then the corresponding flapping frequency, ω_μ , which satisfies the iso-lift condition, is found by solving the following optimization problem,

$$\omega_{\mu} = \underset{\omega}{\operatorname{argmin}} \quad h(p_A, p_{\mu}(\omega))^2,$$
 (17)

where $p_{\mu}(\omega) = (V_{\mu}, \omega, c_{\mu 1}, c_{\mu 2}, c_{\mu 3})$ and $h(p_A, p_{\mu})$ is defined in (13). The above optimization may have multiple solutions; we choose the one below ω_A . Finally, a smooth

TABLE III
TORQUE EXPERIMENTAL PARAMETERS

Flapping Frequency [rad/s]	ω_A	$150.0 \cdot 2\pi$
Trapping Trequency [rad/s]	ω_B	$139.2 \cdot 2\pi$
Operating Voltage [V]	V_A	160.0
Operating voltage [v]	V_B	220.0
	a_1	1.09
	a_2	0
Sinusoid Shape	a_3	0.099
(Harmonic Coefficients)	b_1	0.934
	b_2	0.216
	<i>b</i> ₃	0.047

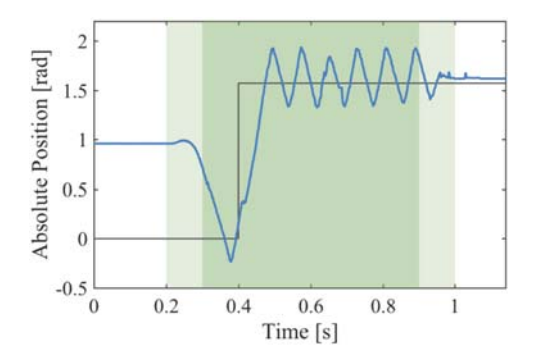


Fig. 10. Step response of the RoboBee using PID control with smooth multimodal control parameter μ . The control signals ramp up and down linearly during testing (light green), but within the section of maximum control authority (dark green), the RoboBee follows the step function with a time constant of 0.1 s.

parameter fit on the numerically-generated list of p_{μ} is used in the following yaw control experiment.

We implemented a PID heading controller with manually-tuned gains using the control parameter μ , with the RoboBee constrained to axial yaw rotation as described in Section III. The reference signal was a heading angle step function, with an initial value of 0 rad and a final value of $\frac{\pi}{2}$ rad. The RoboBee started at an arbitrary angle, and the control signal was ramped as in the yaw torque measurement experiments.

The measured step response is shown in Fig. 10. At full control authority, the RoboBee demonstrated a time constant on the order of 0.1 s, an order of magnitude faster than that demonstrated in [12]. Observing oscillations about the reference signal, we infer that the RoboBee exhibited comparable control authority in both positive and negative yaw torque. While controller optimization will improve the response (e.g., by mitigating the oscillation about the reference signal), we conclude that iso-lift split-cycle yaw torque generation successfully demonstrates substantial yaw control authority.

V. DISCUSSION AND FUTURE WORK

The yaw torque authority achieved by the iso-lift split-cycle method demonstrates sufficient yaw torque for aggressive controlled maneuvers, while maintaining flight-worthy lift. This result was verified by the demonstration of PID heading control, achieving significant performance improvements over previous yaw control attempts. Nevertheless, we must ensure that this method is a viable long-term and robust solution for yaw torque control authority on the RoboBee; this requires further investigation into effects from operating at high voltage conditions and to couple the proposed yaw control strategy with roll and pitch control.

This method of yaw torque generation is particularly favorable because it requires no modification to the existing RoboBee design, which has evolved over the past decade [6]. Therefore, flight performance will not decrease for an MAV with yaw capabilities, nor is any significant effort required to transition between normal flight and yaw domains. We do note, however, that the yaw domain corresponds to lower power efficiency (where efficiency is considered to be the

ratio of lift to power exerted by the actuators; power is directly proportional to $V^2\omega$, for applied voltage V and flapping frequency ω [14]). It follows that iso-lift yaw conditions should be used purposefully during RoboBee flight.

During experiments, the RoboBee flexures wore down to such a degree that the resonant frequency of the MAV dropped approximately 15 Hz. Therefore, operating frequencies which were originally low enough to reduce split-cycle filtering sufficiently to generate yaw torque became too close to the resonant point, and could no longer produce yaw torque. While in practice this can be reversed by replacing worn-down hinges with new, identical copies (a repair which requires only a matter of minutes), this observation indicates that the iso-lift split-cycle method is particularly susceptible to shifts in resonant frequency, and therefore to the state of wear of an individual MAV. It follows that, to achieve robust yaw control, a degree of adaptivity should be integrated into the controller to account for any change in resonance. Additionally, experiments should be conducted to measure any increase in flexure wear due to operation in the lowerefficiency yaw torque domain to anticipate and mitigate deterioration due to operation in yaw conditions.

While simple PID control was successfully demonstrated using iso-lift split-cycle yaw torque generation, a rich area of exploration remains in designing an optimal controller. Performance will be improved by insights into transitions between sinusoid shapes, amplitudes, and frequencies while transitioning from normal flight to yaw conditions, whether independently or as a lumped parameter (as applied herein). Optimization of mode transitions may also decrease flexure deterioration during operation.

Finally, the proposed methods for generating yaw torque sufficient for control authority will be implemented in flight to complement existing control authority in thrust, roll torque, and pitch torque. Not only will this implementation allow a full demonstration of simultaneous yaw torque and lift, but it will open up the expanded set of control parameters used in iso-lift conditions to pave the way for exploration of aggressive control to fully exploit the maneuverability of the RoboBee.

ACKNOWLEDGMENTS

The authors would like to thank Noah Jafferis for assistance in modeling transmission and actuator filtering, and Moritz A. Graule for discussions on validating lift conditions. This work was partially supported by the Office of Naval Research (award #N00014-17-1-2416) and the Wyss Institute for Biologically Inspired Engineering. In addition, the prototypes were enabled by equipment supported by the ARO DURIP program (award #W911NF-13-1-0311). This material is based upon work supported by the National Science Foundation Graduate Research Fellowship Program under Grant No. DGE1745303. Any opinions, findings, and conclusions or recommendations expressed in this material are those of the authors and do not necessarily reflect the views of the National Science Foundation.

REFERENCES

- [1] W. Shyy, C.-k. Kang, P. Chirarattananon, S. Ravi, and H. Liu, "Aerodynamics, sensing and control of insect-scale flapping-wing flight," *Proc. of the Royal Society A: Mathematical, Physical and Engineering Sciences*, vol. 472, no. 2186, p. 20150712, 2016.
- [2] C. T. Orlowski and A. R. Girard, "Dynamics, stability, and control analyses of flapping wing micro-air vehicles," *Progress in Aerospace Sciences*, vol. 51, pp. 18–30, 2012.
- [3] C. P. Ellington, "The novel aerodynamics of insect flight: applications to micro-air vehicles," *Journal of Experimental Biology*, vol. 202, no. 23, pp. 3439–3448, 1999.
- [4] G. De Croon, K. De Clercq, R. Ruijsink, B. Remes, and C. De Wagter, "Design, aerodynamics, and vision-based control of the delfly," *International Journal of Micro Air Vehicles*, vol. 1, no. 2, pp. 71–97, 2009.
- [5] M. Keennon, K. Klingebiel, and H. Won, "Development of the nano hummingbird: A tailless flapping wing micro air vehicle," in 50th AIAA aerospace sciences meeting including the new horizons forum and aerospace exposition, 2012, p. 588.
- [6] R. J. Wood, "Design, fabrication, and analysis of a 3dof, 3cm flapping-wing may," in *Proc. IEEE/RSJ International Conf. on Intelligent Robots and Systems*, 2007, pp. 1576–1581.
- [7] R. Wood, E. Steltz, and R. Fearing, "Optimal energy density piezoelectric bending actuators," *Sensors and Actuators A: Physical*, vol. 119, no. 2, pp. 476–488, 2005.
- [8] K. Y. Ma, P. Chirarattananon, S. B. Fuller, and R. J. Wood, "Controlled flight of a biologically inspired, insect-scale robot," *Science*, vol. 340, no. 6132, pp. 603–607, 2013.
- [9] B. M. Finio and R. J. Wood, "Open-loop roll, pitch and yaw torques for a robotic bee," in *Proc. IEEE/RSJ International Conf. on Intelligent Robots and Systems*, 2012, pp. 113–119.
- [10] N. Gravish and R. J. Wood, "Anomalous yaw torque generation from passively pitching wings," in *Proc. IEEE International Conf.* on Robotics and Automation, 2016, pp. 3282–3287.
- [11] M. W. Oppenheimer, D. B. Doman, and D. O. Sigthorsson, "Dynamics and control of a biomimetic vehicle using biased wingbeat forcing functions," *Journal of guidance, control, and dynamics*, vol. 34, no. 1, pp. 204–217, 2011.

- [12] E. F. Helbling, S. B. Fuller, and R. J. Wood, "Pitch and yaw control of a robotic insect using an onboard magnetometer," in *Proc. IEEE International Conf. on Robotics and Automation*, 2014, pp. 5516–5522
- [13] Z. E. Teoh and R. J. Wood, "A bioinspired approach to torque control in an insect-sized flapping-wing robot," in *Proc. 5th IEEE RAS & EMBS International Conf. on Biomedical Robotics and Biomechatronics*, 2014, pp. 911–917.
- [14] N. T. Jafferis, M. A. Graule, and R. J. Wood, "Non-linear resonance modeling and system design improvements for underactuated flappingwing vehicles," in *Proc. IEEE International Conf. on Robotics and Automation*, 2016, pp. 3234–3241.
- [15] K. Y. Ma, S. M. Felton, and R. J. Wood, "Design, fabrication, and modeling of the split actuator microrobotic bee," in *Proc. IEEE/RSJ International Conf. on Intelligent Robots and Systems*, 2012, pp. 1133–1140.
- [16] P. Chirarattananon, K. Y. Ma, and R. J. Wood, "Adaptive control of a millimeter-scale flapping-wing robot," *Bioinspiration & biomimetics*, vol. 9, no. 2, p. 025004, 2014.
- [17] B. M. Finio, N. O. Pérez-Arancibia, and R. J. Wood, "System identification and linear time-invariant modeling of an insect-sized flapping-wing micro air vehicle," in *Proc. IEEE/RSJ International Conf. on Intelligent Robots and Systems*, 2011, pp. 1107–1114.
- [18] Y. Chen, K. Ma, and R. J. Wood, "Influence of wing morphological and inertial parameters on flapping flight performance," in *Proc. IEEE/RSJ International Conf. on Intelligent Robots and Systems*, 2016, pp. 2329– 2336.
- [19] M. H. Dickinson, F.-O. Lehmann, and S. P. Sane, "Wing rotation and the aerodynamic basis of insect flight," *Science*, vol. 284, no. 5422, pp. 1954–1960, 1999.
- [20] R. Malka, A. L. Desbiens, Y. Chen, and R. J. Wood, "Principles of microscale flexure hinge design for enhanced endurance," in *Proc. IEEE/RSJ International Conf. on Intelligent Robots and Systems*, 2014, pp. 2879–2885.